Cite as: J. Appl. Phys. 131, 153904 (2022); doi: 10.1063/5.0086768

Submitted: 28 January 2022 · Accepted: 7 April 2022 ·

Published Online: 19 April 2022







Thomas J. Peterson, 1 📵 Anthony Hurben, 1 📵 Wei Jiang, 2 📵 Delin Zhang, 2 📵 Brandon Zink, 2 📵 Yu-Chia Chen, 2 Yihong Fan,<sup>2</sup> Tony Low,<sup>2</sup> and Jian-Ping Wang<sup>2,a)</sup> (D

#### **AFFILIATIONS**

- <sup>1</sup>School of Physics and Astronomy, University of Minnesota, Minneapolis, Minnesota 55455, USA
- <sup>2</sup>Electrical and Computer Engineering Department, University of Minnesota, Minneapolis, Minnesota 55455, USA
- <sup>a)</sup>Author to whom correspondence should be addressed: jpwang@umn.edu

#### **ABSTRACT**

Recent advancement in the switching of perpendicular magnetic tunnel junctions with an electric field has been a milestone for realizing bultra-low energy memory and computing devices. To integrate with current spin-transfer torque-magnetic tunnel junction and spin-orbit and torque-magnetic tunnel junction devices, the typical linear fJ/V m range voltage controlled magnetic anisotropy (VCMA) needs to be significantly enhanced with approaches that include new materials or stack engineering. A possible bidirectional and 1.1 pJ/V m VCMA effect has been predicted by using heavily electron-depleted Fe/MgO interfaces. To improve upon existing VCMA technology, we have proposed inserting high work function materials underneath the magnetic layer. This will deplete electrons from the magnetic layer biasing the gating window into the electron-depleted regime, where the pJ/V m and bidirectional VCMA effect was predicted. We have demonstrated tunable 

#### INTRODUCTION

Spintronics offers a new generation of non-volatile, ultrafast memory with current-induced switching utilizing spin-transfer torque (STT)<sup>1-3</sup> and spin-orbit torque (SOT).<sup>4-6</sup> Critical switching current density for these devices remain large in most material systems and methods to reduce the switching energy are highly sought after.7 A potential solution is to utilize the VCMA effect, which allows for a dynamic reduction in magnetic anisotropy with an applied voltage, thus lowering the switching energy while retaining high anisotropy for thermal stability.<sup>8-10</sup> For a ferromagnetic (FM) layer with perpendicular magnetic anisotropy (PMA), the VCMA effect modifies the occupancy of hybridized orbitals at the FM/MgO interface, which are responsible for PMA in the FM layer, thus modifying the magnetic anisotropy. 11,12 Typical CoFeB/ MgO perpendicular magnetic tunnel junction (p-MTJ) systems

show VCMA coefficients ( $\xi$ ) on the order of 10–100 fJ/(V m) for various underlayers. 13-15 To fully reduce the anisotropy energy barrier of thermally stable 10 nm MTJ devices, VCMA coefficients on the order 1–10 pJ/(V m) are required. <sup>16</sup> Additionally, direct STT applications are limited by linear VCMA responses which, while decreasing the switching energy in one direction of applied voltage, increases the energy for the other direction. 13,14 Recent theoretical work by Zhang et al. for Fe/MgO systems has predicted a large [~1 pJ/(V m)] and bidirectional effect at high levels of electron depletion.<sup>17</sup> However, the required voltages to achieve these levels of depletion are beyond the dielectric breakdown of experimental gates.

In this paper, we utilize a Ta/Pd(x)/Ta underlayer to create a tunable metal-metal junction to reach levels of electron depletion at the interfaces not possible with only applied voltages. 18 When a ferromagnetic layer is brought into contact with the underlayer due

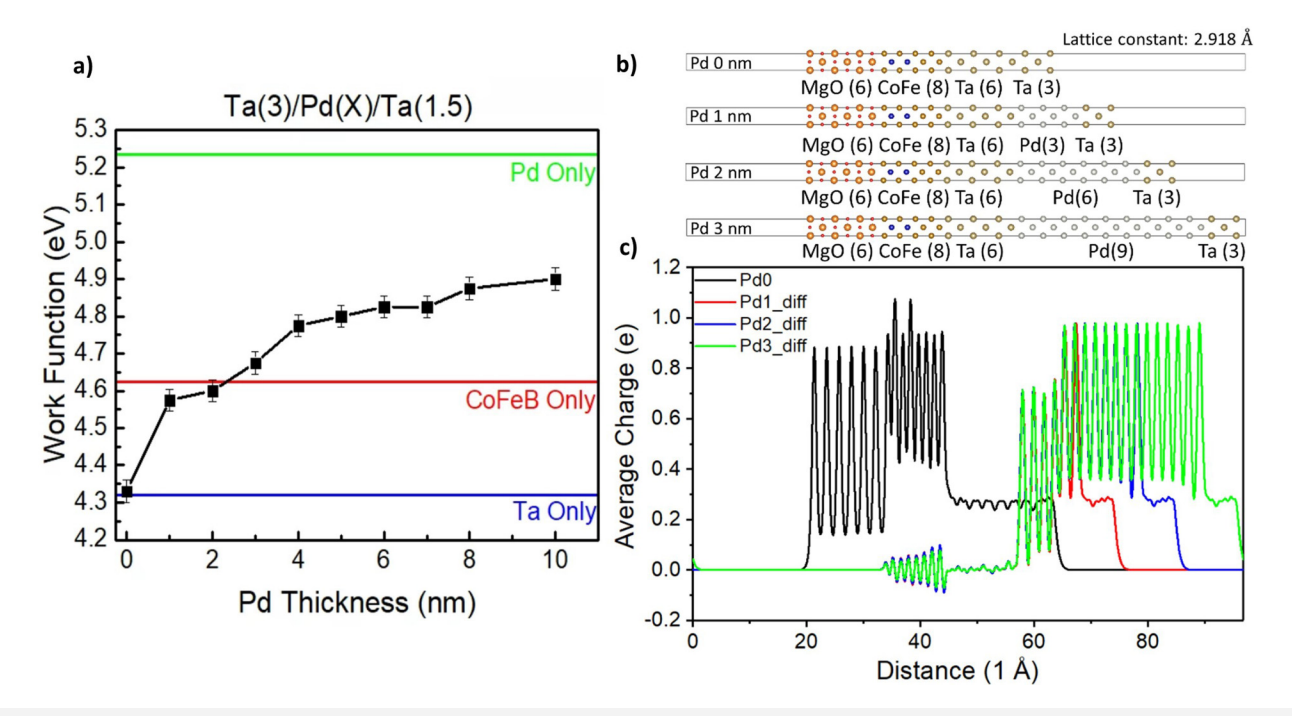


FIG. 1. (a) UPS measurements of the underlayer vacuum etched to Ta 1 nm. Green lines show measured values control samples of oxide etched 20 nm Ta, Pd, and CoFeB films. (b) Slab structure for the first-principles calculations and (c) the plane-averaged charge of Pd 0 slab and the charge difference of the Pd 1, 2, 3 nm slabs from the Pd 0 slab.

to the difference in work functions, the Fermi levels will equalize creating an effective built-in voltage drop. 19-22 Utilizing varied Pd thicknesses from 0 to 10 nm, the underlayer's work function becomes tunable, allowing for a larger range of electron depletion than can be reached with only an applied gate voltage. By using ultraviolet photoelectron spectroscopy (UPS), we have demonstrated the work function tunability of the Ta/Pd(x)/Ta underlayers. To investigate the extent of the electron depletion as a function of the Pd thickness in the underlayer, we have performed DFT calculations on supercells of Ta/Pd(x)/Ta/CoFe/MgO, which demonstrate that the electron depletion will not be fully screened at the CoFe/MgO interface. Gated pillar devices with Hall cross geometries were fabricated and tested to extract the anisotropy change as a function of applied gate voltage for samples with various Pd thicknesses. The electron-depleted Pd samples show a three to six times VCMA improvement compared to the electron accumulated Ta control sample.

# VIABILITY OF A TUNABLE ELECTRON DEPLETION UNDERLAYER

The work function tunablity of the Ta/Pd(x)/Ta underlayer was demonstrated via ultraviolet photon spectroscopy (UPS) measurements in ultrahigh vacuum. Isolated stacks of  $SiO_2/Ta(3 \text{ nm})/Pd(x \text{ nm})/Ta(5 \text{ nm})$  were grown using magnetron sputtering on 300 nm thermally oxidized Si substrates with a base pressure of

9 × 10<sup>-8</sup> Torr and an Ar working pressure of 1.5 mTorr. The films were then annealed at 300 °C for 30 min in the nitrogen environment. Via *in situ* ion milling and x-ray photoelectron spectroscopy (XPS), the top 3.5 nm of TaOx was removed, leaving a 1.5 nm unoxidized Ta interface. Additional annealed stacks of isolated 20 nm Ta, Pd, and CoFeB were grown to measure the baseline polycrystalline work function values of the sputtered films, with any oxide fully etched away before measurement. By varying the Pd thickness, a wide range of work functions can be tuned, varying from 4.32 to 4.90 eV, as shown in Fig. 1(a). For Pd thicknesses of 0–2 nm, we observe electron accumulation in the CoFeB layer with a work function of 4.63 eV. Thicknesses above 3 nm show increasing electron depletion behavior saturating to 4.90 eV, well below the isolated Pd value of 5.24 eV.

To better understand the underlying physical origin and extent of the depletion effect, first-principles calculations of (MgO)<sub>6</sub> (CoFe)<sub>8</sub> Ta<sub>3</sub>Pd<sub>y</sub>Ta<sub>6</sub>, where <sub>y</sub> is the number of atomic monolayers based on the density functional theory (DFT) were performed. The lattice constant of MgO (2.918 Å) was adopted for the slab calculation with a vacuum layer thicker than 20 Å to avoid the interactions between slabs. CoFe is used in place of CoFeB for the calculation to better represent the experimental films with boron diffusion into the Ta layer and CoFe crystallization after annealing.<sup>23</sup> A diagram of the slabs is shown in Fig. 1(b), the 0, 3, 6, and 9 monolayer Pd slabs are labeled as Pd 0, 1, 2, and 3 nm, respectively. The generalized gradient approximation exchange-correlation potentials plus the

projector augmented wave method for the electron-ion interaction<sup>24</sup> were implemented in Vienna ab initio simulation package code.<sup>25</sup> All self-consistent calculations were performed with a plane wave cutoff of 500 eV. The geometric optimizations were carried out without any constraint until the force on each atom was less than 0.01 eV/Å and the change of energy per cell was smaller than 10<sup>-5</sup> eV. The Brillouin zone k-point sampling was set with a 12×12×1 Γ-centered Monkhorst-Pack grids. To better describe the localized 3d electrons of transition metal, an additional on-site Hubbard-U correction term was applied with the different U values tested.<sup>26</sup> The dipole correction was applied to properly treat the dipole moment due to the formation of heterostructures. To get the change of the plane-averaged charge (PAC) profile due to the change of the Pd thickness, the PAC of different heterostructures were aligned with each other in the vacuum and compared between different structures. Figure 1(c) depicts the PAC of the Pd 0 slab and the charge difference of the Pd 1, 2, 3 nm slabs from the Pd 0 slab. The MgO slab starts after 20 Å vacuum layer then is followed by the CoFe and Ta/Pd(x)/Ta layers. The charge difference in the vacuum and MgO layers is zero, however, in the CoFe layer of the Pd 1, 2, 3 slabs, there is a decaying charge profile as expected. The charge difference is the largest at the CoFe/Ta interface and decays due to the electron screening in the metal layer. The charge difference remains nonzero at the MgO/CoFe interface, which dominates the anisotropy and VCMA response, suggesting there will be an effect on the VCMA due to the electron depletion from the Pd layer.

#### MATERIALS GROWTH AND CHARACTERIZATION

Films of Ta (3 nm)/Pd (2, 4, 6, 8, 10 nm)/Ta (1.5 nm)/  $Co_{20}Fe_{60}B_{20}$  (1.3 nm)/MgO (2.2 nm)/Ta (2 nm) as well as a Ta control sample of Ta (5 nm)/Co $_{20}Fe_{60}B_{20}\ (1.3\ nm)/MgO\ (2.2\ nm)/$ Ta (2 nm) were deposited via magnetron sputtering, using the same conditions as above, for magnetic and electrical testing. The 2 nm Ta capping layer is naturally oxidized after removal from the sputtering system, forming a 2 nm TaOx film. The films were then annealed at 300 °C for 30 min. The bottom Ta (3 nm) layer provides adhesion of the Pd to the SiO<sub>2</sub> substrate while the 1.5 nm Ta layer helps nucleate the body-centered cubic form of the CoFeB allowing for interfacial PMA. PMA was confirmed for all Pd thicknesses up to 10 nm via vibrating sample magnetometer (VSM) measurements shown in Fig. 3(a). The squareness of the perpendicular loop and strength of the anisotropy decreases for the Pd 10 nm sample. Tunneling electron microscope (TEM) measurements were done on the Pd 2 and 10 nm samples. Bright-field TEM and 8 High-Angle Annular Dark-Field (HAADF) images of Pd 10 and Pd ₹ 2 nm samples are shown in Fig. 2. The TEM shows polycrystalline Ta, Pd, CFB, and MgO layers with large grains in the Pd layer on the scale of the film thickness for the Pd 10 nm sample. The formation of these large Pd grains likely increased the roughness of the

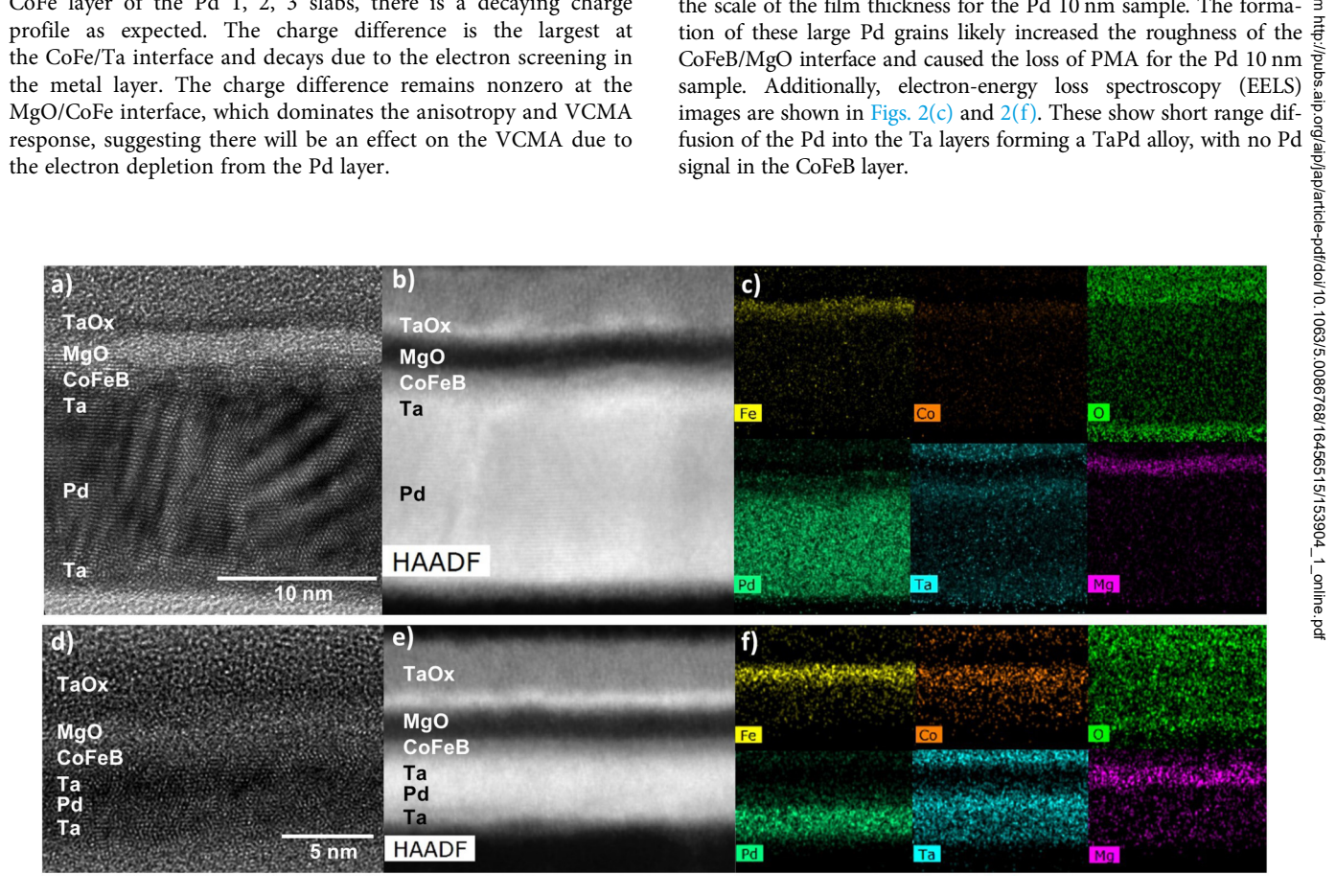


FIG. 2. (a) Bright-field TEM, (b) high-angle annular dark-field TEM, (c) EELS elemental mapping of the Pd 10 nm sample. (d) Bright-field TEM, (e) high-angle annular dark-field TEM, (f) EELS elemental mapping of the Pd 2 nm sample.

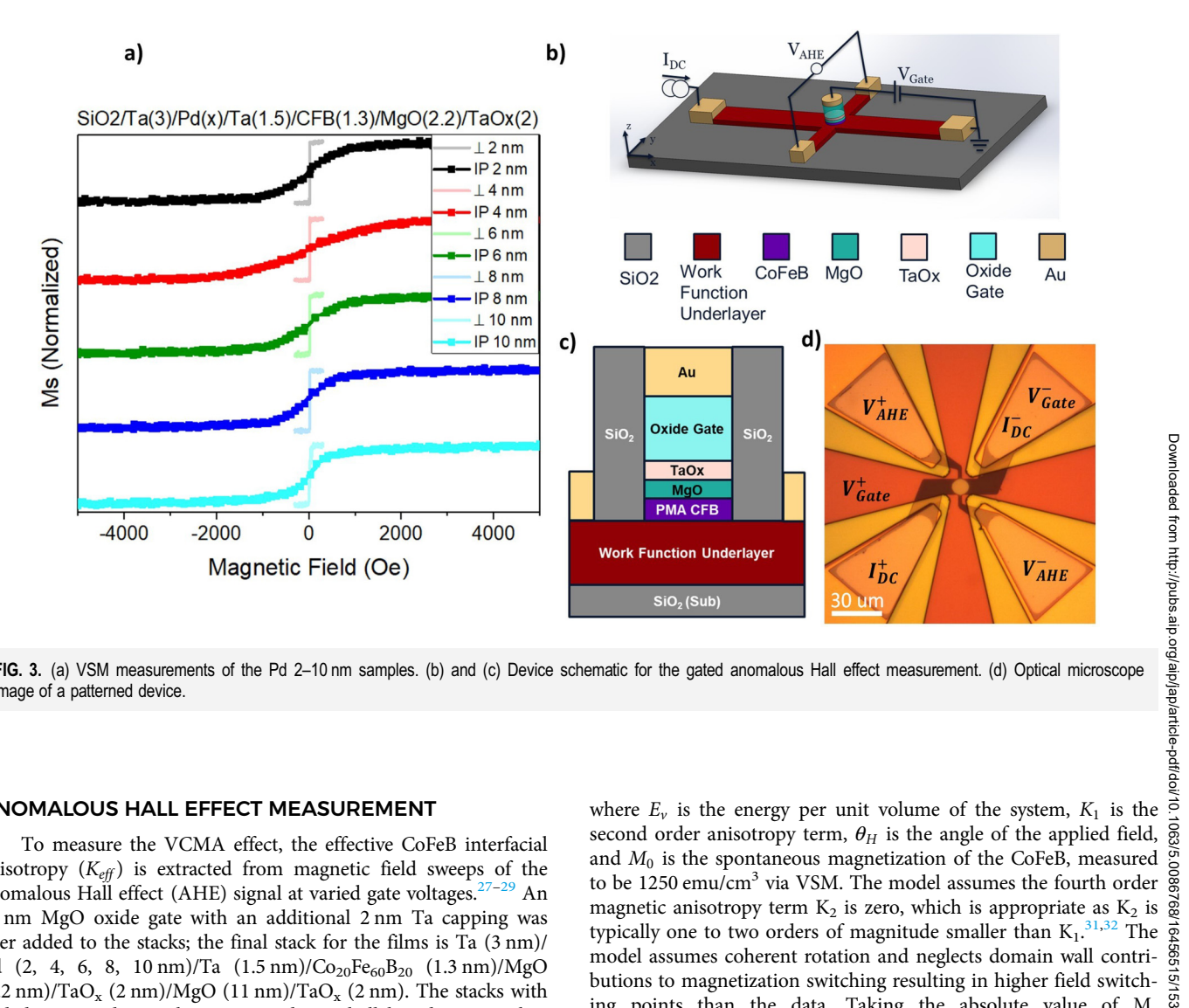


FIG. 3. (a) VSM measurements of the Pd 2-10 nm samples. (b) and (c) Device schematic for the gated anomalous Hall effect measurement. (d) Optical microscope image of a patterned device.

#### ANOMALOUS HALL EFFECT MEASUREMENT

To measure the VCMA effect, the effective CoFeB interfacial anisotropy  $(K_{eff})$  is extracted from magnetic field sweeps of the anomalous Hall effect (AHE) signal at varied gate voltages. 27-29 An 11 nm MgO oxide gate with an additional 2 nm Ta capping was later added to the stacks; the final stack for the films is Ta (3 nm)/ Pd (2, 4, 6, 8, 10 nm)/Ta (1.5 nm)/Co<sub>20</sub>Fe<sub>60</sub>B<sub>20</sub> (1.3 nm)/MgO (2.2 nm)/TaO<sub>x</sub> (2 nm)/MgO (11 nm)/TaO<sub>x</sub> (2 nm). The stacks with added gate oxide are then patterned into hall bar devices with a 7 μm diameter gated pillar in the hall cross. The CFB/MgO/TaO<sub>x</sub>/ MgO/TaO<sub>x</sub> layers outside the pillar were removed via ion milling, and the pillar was insulated utilizing a 200 nm PE-CVD grown  $SiO_x$  layer. A device schematic is shown in Figs. 3(b)-3(d). The Pd 10 nm sample was not electrically tested for VCMA due to the weakened PMA. A DC current is applied through the Hall channel with a magnetic field ranging from 0.75 to -0.75 T along the in-plane direction of CoFeB. The transverse voltage is measured to extract the AHE signal as a function of applied field, as seen in Fig. 4(a). The AHE voltages are normalized by taking the maximal (minimal) value to represent  $M_z = +1$  (-1). The resulting magnetization tilting,  $\theta_M$ , due to the applied field can be numerically modeled using the Stoner-Wohlfarth model<sup>30</sup>

$$E_{\nu} = K_1 \sin^2(\theta_M - \theta_H) - M_0 H \cos \theta_M$$

butions to magnetization switching resulting in higher field switch-  $\frac{1}{2}$ ing points than the data. Taking the absolute value of M<sub>z</sub> and normalization removes the switching points, allowing for accurate the switching points, allowing for accurate the switching points, allowing for accurate the switching points are sufficiently as the switching points and sufficiently as the switching points are curve fitting. Additionally, the normalized AHE curves can be fit using the modeled  $\theta_{M(H)}$  to estimate the anisotropy  $K_1$  using

$$|V| = \beta_{AHE} |\cos \theta_M| + \beta_{PHE} |\sin \theta_M|,$$

where  $\beta_{AHE}$  and  $\beta_{PHE}$  are the voltages resulting from the anomalous Hall and planar Hall effects, respectively. This is repeated as the gating voltage is swept from -4 to +4 V to estimate the change in K<sub>1</sub> as a function of applied voltage. The gate voltage is stepped in 0.4 V increments from negative to positive values and is then retraced from positive to negative to ensure there are no hysteretic effects from ionic motion. The VCMA coefficient  $\xi_{VCMA}$  can be extracted from the derivative of effective interfacial anisotropy with respect to the electric field at the MgO/CoFeB interface for a linear

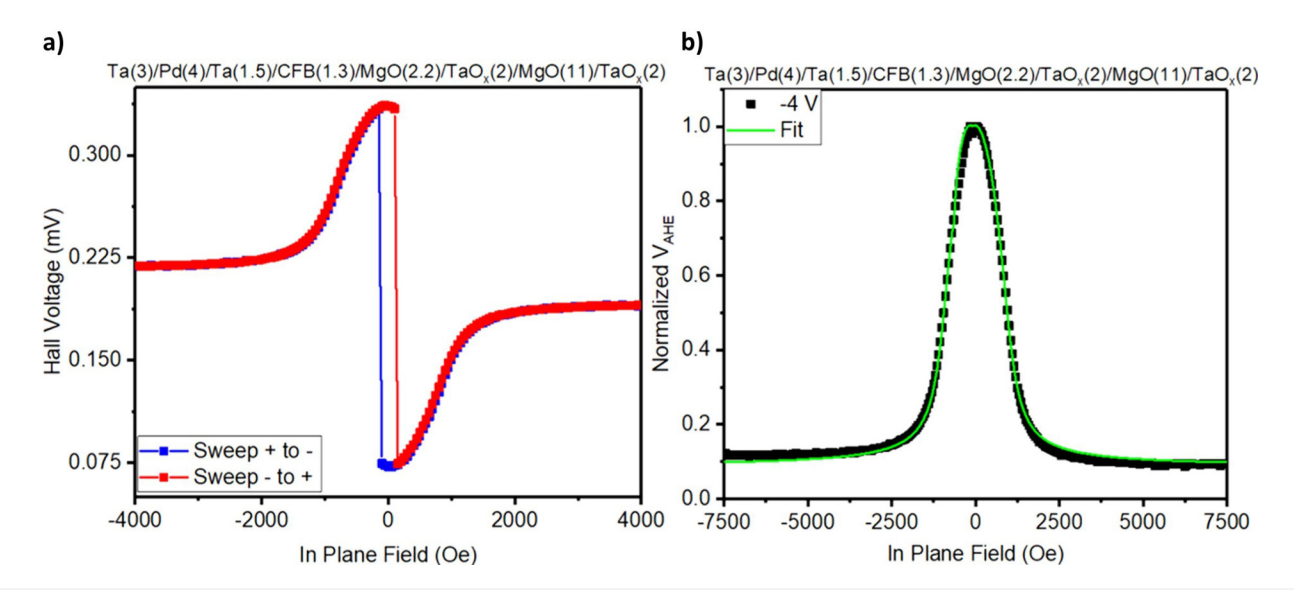


FIG. 4. (a) Anomalous Hall effect (AHE) voltage of the Pd 4 nm sample as an in-plane field is swept from positive to negative fields (blue curve) and negative to positive fields (red curve). (b) Fitted magnetization curve of the normalized and subtracted AHE voltage for the Pd 4 nm sample with an applied -0.4 V gate voltage.

VCMA effect this takes the form of

$$\xi_{VCMA} = \frac{t_{gate}}{V} K_1 t_{FM},$$

where  $t_{gate}$  and  $t_{FM}$  are the thicknesses of the MgO gate and the ferromagnetic CoFeB layer, respectively. The  $t_{FM}$  term also accounts for the magnetic dead layer extracted from the VSM sheet films samples. The extracted  $K_1/M_o$  for the Ta control sample and Pd 2,4,6,8 nm samples are shown in Figs. 5(a)-5(e). All samples appear linear with voltage. The Pd based films have three to six times larger  $\xi_{VCMA}$  than the Ta the control sample, with a peak VCMA coefficient of -16.8 fJ/V m for the Pd 2 nm sample. Plotting  $\xi_{VCMA}$  vs the difference in work function of the CFB and underlayer allows for comparing to the electron-depleted VCMA predictions in Fe/MgO by Zhang et al.<sup>17</sup> The heavily electron accumulated Ta control sample has a small negative sign, -3 fJ/V m VCMA coefficient. As the Pd thickness is increased and, therefore, the electron concentration in the CFB decreases, we see a sharp increase in the VMCA coefficient as the CFB goes from electron accumulation to a neutral state. Then, as the CFB goes from neutral to electron depletion, we see a gradual decrease in magnitude of the VCMA coefficient toward 0 where the bidirectional point is predicted. At even further levels of electron depletion, we would expect to see the bidirectional VCMA as well as increasing positive VCMA coefficients until the peak pJ/V m VCMA coefficient is reached. However, the sign of the VCMA coefficient remains negative for all Pd thicknesses, higher work functions and, therefore, higher levels of electron depletion are needed to realize the bidirectional and pJ/V m effect predicted in the Fe/MgO system. The Ta/Pd(x)/Ta underlayer work function, which saturates to only 4.9 eV, is too low to reach the levels of electron depletion needed. Engineering a new underlayer with a phigher work function material, such as Pt with a work function of 5.64 eV, may allow for realizing the bidirectional and pJ/V m VCMA coefficients. The trend of the VCMA coefficient with the level of electron concentration appears to qualitatively match the predictions; however, the magnitude of the VMCA effect is smaller than expected. The Ta control sample demonstrates a much smaller VCMA coefficient than the literature values of 14–33 fJ/V m<sup>14,27,33,34</sup> for typical Ta/CoFeB/MgO systems. This is likely due to the low ordering of the polycrystalline CoFeB/MgO interfaces grown within these samples. Improving the crystallinity and PMA quality of the samples will likely improve the VCMA coefficient.

VCMA coefficient.

The work function tunablity of the Ta/Pd/Ta underlayer with the improved VCMA effect paves the way for designing new and more efficent spin torque based MRAM. For use in STT-MRAM a second to the state of the large and bidirectional VCMA effect must be realized. The proposed structure can be easily implemented into existing STT devices, while retaining PMA in the ferromagnetic layer, crucial for device scaling. With a combined VCMA + STT device the applied switching current also produces a voltage across the insulating barrier of the p-MTJ, temporarily lowering the magnetic anisotropy allowing for reduced switching current. After switching, the anisotropy returns to a larger value allowing for thermal stability. In SOT-MRAM, the geometry of the devices allows for the use of the unidirectional VCMA effect observed in the samples. For integration of the proposed structure, it is ideal for the electron depletion underlayer to serve also as the spin hall channel. Pd is not an ideal spin Hall material, having a realitivly low spin torque efficiency up to 0.01;<sup>35–37</sup> however, the Ta/Pd/Ta underlayer can be easily replaced with an alternative high work function and high efficiency SOT material while maintaining the electron depletion from the

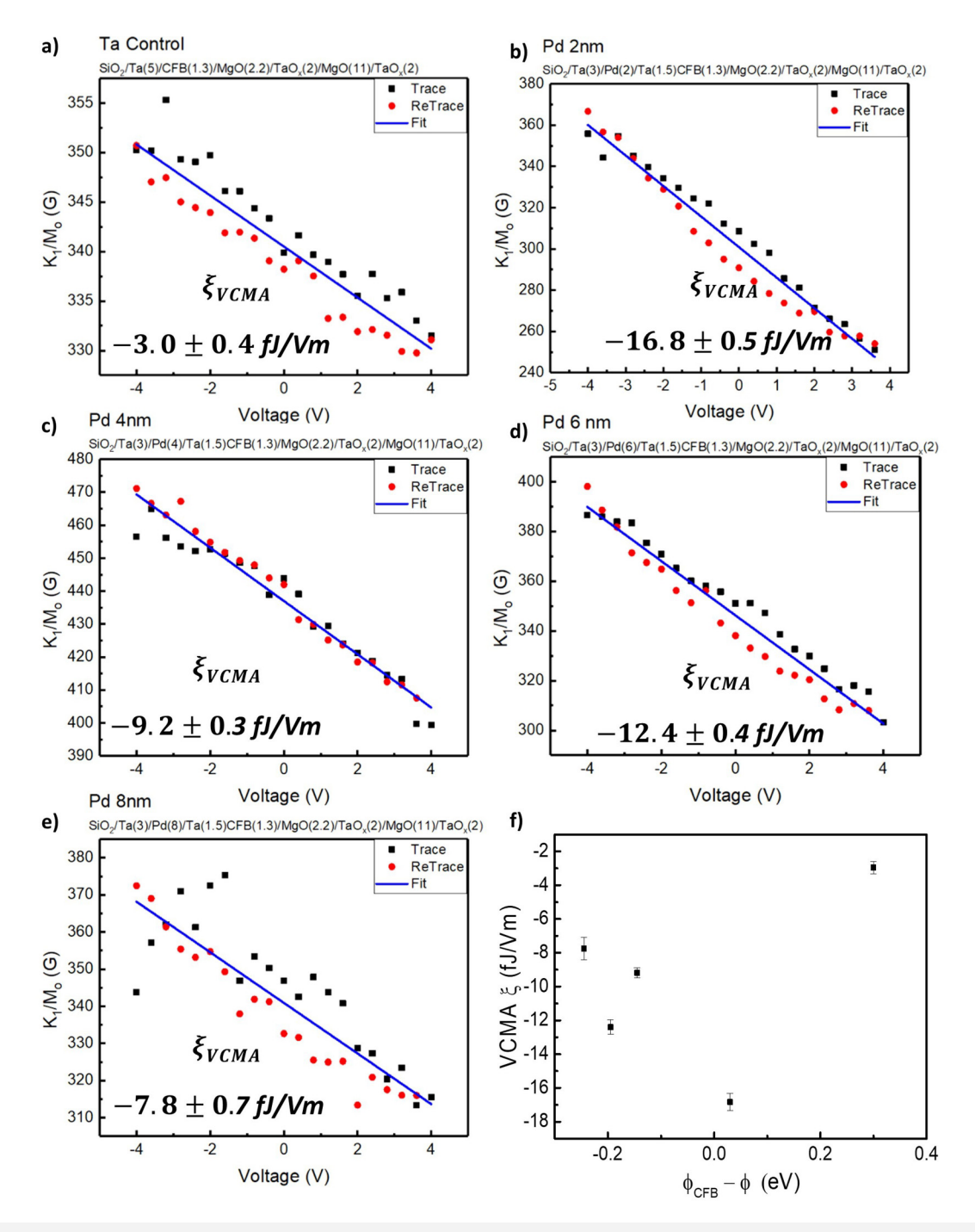


FIG. 5. (a)–(e) Extracted K<sub>1</sub> and linear fits of Ta control and Pd 2,4,6,8 nm samples. (f) Resulting VCMA response of the Ta control sample and the Pd underlayers plotted against the effective work function difference of the underlayer with respect to the CFB layer.

underlayer stack. A promising candiate is Pt and Pt alloys, which has a workfuction higher than that of Pd. Recent reports have shown spin torque efficiencies of 0.12,<sup>38</sup> 0.26,<sup>39</sup> and 0.3<sup>40</sup> for Pt, Pd<sub>25</sub>Pt<sub>75</sub>, and Au<sub>25</sub>Pt<sub>75</sub>, respectively. Another promising candiate to

replace Ta/Pd/Ta for SOT + VCMA devices are topological insulators (TIs), such as  $\rm Bi_2Se_3,^{41-47}$  ( $\rm Bi_xSb_y)_2Te_3,^{48,49}$  and  $\rm Bi_2Te_3,^{48}$  These TI systems have shown spin torque efficiencies much greater than seen in heavy metals with demonstrated work functions as

#### CONCLUSIONS

The bidirectional and pJ/V m range VCMA coefficients predicted by Zhang et al. 17 require heavily electron-depleted FM layers. The electric fields required to reach these levels of electron depletion are well beyond what is possible with dielectric gating alone. In this paper, we utilized Ta (3 nm)/Pd (2, 4, 6, 8 nm)/Ta (1.5 nm) underlayers to provide a built-in biasing to a CoFeB FM layer through the work function mismatch at the metal-metal junction. Through UPS measurements, we have demonstrated tunable control of the Ta/Pd/Ta structure's work function with the Pd thickness. To verify the electron depletion is not electronically screened within the FM layer, DFT calculations were performed on supercells of Ta/Pd(x)/Ta/CoFe/MgO. The calculations demonstrate a decaying charge profile in CoFe that is non-zero at the CoFe/ MgO interface. Devices were fabricated for gated AHE measurements to extract the anisotropy and VCMA coefficient of Ta/Pd/ Ta/ stacks as well as a Ta control sample. The VCMA coefficients of the Pd based samples show an improvement over the Ta control sample and qualitatively match the trends predicted as the electron concentration is decreased. However, the predicted bidirectional and pJ/V m range VCMA effect was not observed. High work function underlayer materials are required to reach the levels of electron depletion needed to observe the effects. The proposed tunable work function structure for improving VMCA can be easily integrated with existing STT- and SOT-MRAM devices provided the underlayer materials can be engineered to achieve a higher work function than CoFeB.

### **ACKNOWLEDGMENTS**

This work was supported, in part, by ASCENT, one of the six centers in JUMP, a Semiconductor Research Corporation (SRC) program sponsored by DARPA. This material is based upon work supported, in part, by the National Science Foundation under the Scalable Parallelism in the Extreme (SPX) Grant under Award No. CCF-1725420. Y. Fan, Dr. W. Jiang, and Dr. T. Low are supported by the SMART, one of the seven centers of nCORE, a Semiconductor Research Corporation program, sponsored by the National Institute of Standards and Technology (NIST). The TEM was performed by Dr. Jason Myers at the College of Science and Engineering (CSE) Characterization Facility at the University of Minnesota (UMN), supported, in part, by the NSF through the UMN MRSEC program. Portions of this work were conducted in the Minnesota Nano Center, which is supported by the National Science Foundation through the National Nano Coordinated Infrastructure Network (NNCI) under Award No. ECCS-2025124.

## **AUTHOR DECLARATIONS** Conflict of Interest

The authors have no conflicts to disclose.

#### **DATA AVAILABILITY**

The data that support the findings of this study are available from the corresponding author upon reasonable request.

#### **REFERENCES**

- <sup>1</sup>K. Ando, S. Fujita, J. Ito, S. Yuasa, Y. Suzuki, Y. Nakatani, T. Miyazaki, and H. Yoda, J. Appl. Phys. 115, 172607 (2014).
- <sup>2</sup>A. V. Khvalkovskiy, D. Apalkov, S. Watts, R. Chepulskii, R. S. Beach, A. Ong, X. Tang, A. Driskill-Smith, W. H. Butler, P. B. Visscher, D. Lottis, E. Chen, V. Nikitin, and M. Krounbi, J. Phys. D: Appl. Phys. 46, 074001 (2013).
- <sup>3</sup>J. P. Wang, S. S. Sapatnekar, C. H. Kim, P. Crowell, S. Koester, S. Datta, K. Roy, A. Raghunathan, X. S. Hu, M. Niemier, A. Naeemi, C. L. Chien, C. Ross, and R. Kawakami, in Proceedings—Design Automation Conference (ACM, New York, 2017), pp. 1-6.
- <sup>4</sup>I. M. Miron, K. Garello, G. Gaudin, P.-J. Zermatten, M. V. Costache, S. Auffret, S. Bandiera, B. Rodmacq, A. Schuhl, and P. Gambardella, Nature 476, 189-193 (2011).
- <sup>5</sup>S. Manipatruni, D. E. Nikonov, and I. A. Young, Appl. Phys. Express 7, 103001
- <sup>6</sup>L. Liu, C.-F. Pai, Y. Li, H. W. Tseng, D. C. Ralph, and R. A. Buhrman, Science 336, 555-558 (2012).
- <sup>7</sup>T. Nozaki, T. Yamamoto, S. Miwa, M. Tsujikawa, M. Shirai, S. Yuasa, and Y. Suzuki, Micromachines 10, 327 (2019).
- <sup>8</sup>C.-G. Duan, S. S. Jaswal, and E. Y. Tsymbal, Phys. Rev. Lett. **97**, 47201 (2006).

  <sup>9</sup>M. Weisheit, S. Fähler, A. Marty, Y. Souche, C. Poinsignon, and D. Givord, Science 315, 349-351 (2007).
- 10 T. Maruyama, Y. Shiota, T. Nozaki, K. Ohta, N. Toda, M. Mizuguchi, A. A. Tulapurkar, T. Shinjo, M. Shiraishi, S. Mizukami, Y. Ando, and Y. Suzuki, Nat. Nanotechnol. 4, 158-161 (2009).
- <sup>11</sup>K. H. He, J. S. Chen, and Y. P. Feng, Appl. Phys. Lett. **99**, 072503 (2011).
- <sup>12</sup>M. K. Niranjan, C.-G. Duan, S. S. Jaswal, and E. Y. Tsymbal, Appl. Phys. Lett. 96, 222504 (2010).
- 13 T. Nozaki, A. Kozioł-Rachwał, W. Skowroński, V. Zayets, Y. Shiota, S. Tamaru, H. Kubota, A. Fukushima, S. Yuasa, and Y. Suzuki, Phys. Rev. Appl. 5, 44006
- (2016).

  14Y. Shiota, F. Bonell, S. Miwa, N. Mizuochi, T. Shinjo, and Y. Suzuki, Appl.

  Phys. Lett. 103, 082410 (2013).

  15W. Skowroński, T. Nozaki, Y. Shiota, S. Tamaru, K. Yakushiji, H. Kubota, A. Fukushima, S. Yuasa, and Y. Suzuki, Appl. Phys. Express 8, 053003 (2015).
- A. Fukushima, S. Yuasa, and Y. Suzuki, Appl. Phys. Express 8, 053003 (2015).
- A. Fukushima, S. Yuasa, and Y. Suzuki, Appl. Phys. Express 8, 053003 (2015).

  16P. K. Amiri, J. G. Alzate, X. Q. Cai, F. Ebrahimi, Q. Hu, K. Wong, C. Grèzes, H. Lee, G. Yu, X. Li, M. Akyol, Q. Shao, J. A. Katine, J. Langer, B. Ocker, and Y. L. Wong, IEEE Trans. Many 51 (2015). K. L. Wang, IEEE Trans. Magn. 51, ■ (2015).
- T. L. Wang, IEEE Trans. Magn. 51, (2015).

  75 J. Zhang, P. V. Lukashev, S. S. Jaswal, and E. Y. Tsymbal, Phys. Rev. B 96, (2017).
- 18 J.-P. Wang, T. J. Peterson, A. W. Hurben, and D. Zhang, 17/249,105 (2021).
- 18 J.-P. Wang, T. J. Peterson, A. W. Hurben, and D. Zhang, 17/249,105 (2021).
   19 L. L. Chu, K. Takahata, P. R. Selvaganapathy, Y. B. Gianchandani, and English a J. L. Shohet, J. Microelectromech. Syst. 14, 691 (2005).
- 20 C.-H. Lu, G. M. T. Wong, M. D. Deal, W. Tsai, P. Majhi, C. O. Chui, M. R. Visokay, J. J. Chambers, L. Colombo, B. M. Clemens, and Y. Nishi, IEEE Electron Device Lett. 26, 445-447 (2005).
- <sup>21</sup>G. Giovannetti, P. A. Khomyakov, G. Brocks, V. M. Karpan, J. Van Den Brink, and P. J. Kelly, Phys. Rev. Lett. 101, 26803 (2008).
- <sup>22</sup>H. Lu, Z. Liu, X. Yan, D. Li, L. Parent, and H. Tian, Sci. Rep. 6, 1 (2016).
- <sup>23</sup>X. D. Xu, K. Mukaiyama, S. Kasai, T. Ohkubo, and K. Hono, Acta Mater. 161,
- <sup>24</sup>J. P. Perdew, K. Burke, and M. Ernzerhof, Phys. Rev. Lett. 77, 3865–3868 (1996).
- **25**G. Kresse and J. Hafner, Phys. Rev. B **47**, 558–561 (1993).
- <sup>26</sup>O. Bengone, M. Alouani, P. Blöchl, and J. Hugel, Phys. Rev. B 62, 16392-16401 (2000).
- <sup>27</sup>M. Endo, S. Kanai, S. Ikeda, F. Matsukura, and H. Ohno, Appl. Phys. Lett. 96, 212503 (2010).

<sup>29</sup>X. Li, G. Yu, H. Wu, P. V. Ong, K. Wong, Q. Hu, F. Ebrahimi, P. Upadhyaya, M. Akyol, N. Kioussis, X. Han, P. Khalili Amiri, and K. L. Wang, Appl. Phys. Lett. 107, 142403 (2015).

30 E. C. Stoner and E. P. Wohlfarth, Philos. Trans. R. Soc. London Ser., A 240, 599 (1948).

 $^{\bf 31}$  J. M. Shaw, H. T. Nembach, M. Weiler, T. J. Silva, M. Schoen, J. Z. Sun, and D. C. Worledge, IEEE Magn. Lett. 6, ■ (2015).

<sup>32</sup>M. S. Gabor, T. Petrisor, O. Pop, S. Colis, and C. Tiusan, J. Magn. Magn. Mater. 392, 79–82 (2015).

<sup>33</sup>Y.-C. Lau, P. Sheng, S. Mitani, D. Chiba, and M. Hayashi, Appl. Phys. Lett. 110, 022405 (2017).

<sup>34</sup>J. G. Alzate, P. Khalili Amiri, G. Yu, P. Upadhyaya, J. A. Katine, J. Langer, B. Ocker, I. N. Krivorotov, and K. L. Wang, Appl. Phys. Lett. 104, 112410 (2014).

35X. D. Tao, Z. Feng, B. F. Miao, L. Sun, B. You, D. Wu, J. Du, W. Zhang, and H. F. Ding, J. Appl. Phys. 115, 17C504 (2014).

<sup>36</sup>K. Ando and E. Saitoh, J. Appl. Phys. **108**, 113925 (2010).

<sup>37</sup>K. Harii, K. Ando, K. Sasage, and E. Saitoh, Phys. Status Solidi C 4, 4437–4440 (2007).

<sup>38</sup>C.-F. Pai, Y. Ou, L. H. Vilela-Leão, D. C. Ralph, and R. A. Buhrman, Phys. Rev. B **92**, 64426 (2015).

<sup>39</sup>L. Zhu, K. Sobotkiewich, X. Ma, X. Li, D. C. Ralph, and R. A. Buhrman, Adv. Funct. Mater. 29, 1805822 (2019).

40 L. Zhu, D. C. Ralph, and R. A. Buhrman, Phys. Rev. Appl. 10, 31001 (2018).

<sup>41</sup>A. R. Mellnik, J. S. Lee, A. Richardella, J. L. Grab, P. J. Mintun, M. H. Fischer, A. Vaezi, A. Manchon, E.-A. Kim, N. Samarth, and D. C. Ralph, Nature 511, 449–451 (2014).

<sup>42</sup>Y. Wang, P. Deorani, K. Banerjee, N. Koirala, M. Brahlek, S. Oh, and H. Yang, Phys. Rev. Lett. 114, 257202 (2015).

<sup>43</sup>M. Jamali, J. S. Lee, J. S. Jeong, F. Mahfouzi, Y. Lv, Z. Zhao, B. K. Nikolić, K. A. Mkhoyan, N. Samarth, and J.-P. Wang, Nano Lett. 15, 7126–7132 (2015).

<sup>44</sup>M. DC, R. Grassi, J.-Y. Chen, M. Jamali, D. Reifsnyder Hickey, D. Zhang, Z. Zhao, H. Li, P. Quarterman, Y. Lv, M. Li, A. Manchon, K. A. Mkhoyan, T. Low, and J.-P. Wang, Nat. Mater. 17, 800–807 (2018).

<sup>45</sup>M. DC, T. Liu, J.-Y. Chen, T. Peterson, P. Sahu, H. Li, Z. Zhao, M. Wu, and J.-P. Wang, Appl. Phys. Lett. **114**, 102401 (2019).

<sup>46</sup>R. Ramaswamy, T. Dutta, S. Liang, G. Yang, M. S. M. Saifullah, and H. Yang, J. Phys. D: Appl. Phys. **52**, 224001 (2019).

<sup>47</sup>M. DC, J.-Y. Chen, T. Peterson, P. Sahu, B. Ma, N. Mousavi, R. Harjani, and J.-P. Wang, Nano Lett. **19**, 4836–4844 (2019).

48K. Kondou, R. Yoshimi, A. Tsukazaki, Y. Fukuma, J. Matsuno, K. S. Takahashi, M. Kawasaki, Y. Tokura, and Y. Otani, Nat. Phys. 12, 1027–1031 (2016).

Y. Tserkovnyak, and K. L. Wang, Nat. Mater. 13, 699–704 (2014).

50D. Takane, S. Souma, T. Sato, T. Takahashi, K. Segawa, and Y. Ando, Appl. Phys. Lett. 109, 091601 (2016).